Microscale Transport Phenomena in Materials Processing

Yogesh Jaluria
Board of Governors Professor
Mechanical and Aerospace Engineering
Department,
Rutgers University,
Piscataway, NJ 08854
e-mail: jaluria@jove.rutgers.edu

Microscale transport mechanisms play a critical role in the thermal processing of materials because changes in the structure and characteristics of the material largely occur at these or smaller length scales. The heat transfer and fluid flow considerations determine the properties of the final product, such as in a crystal drawn from silicon melt or a gel from the chemical conversion of a biopolymer. Also, a wide variety of material fabrication processes, such as the manufacture of optical glass fiber for telecommunications, fabrication of thin films by chemical vapor deposition, and surface coating, involve microscale length scales due to the requirements on the devices and applications for which they are intended. For example, hollow fibers, which are used for sensors and power delivery, typically need fairly precise microscale wall thicknesses and hole diameters for satisfactory operation. The basic transport mechanisms underlying these processes are discussed in this review paper. The importance of material characterization in accurate modeling and experimentation is brought out, along with the coupling between the process and the resulting properties such as uniformity, concentricity, and diameter. Of particular interest are thermally induced defects and other imperfections that may arise due to the transport phenomena involved at these microscale levels. Additional aspects such as surface tension, stability, and free surface characteristics that affect the material processing at microscale dimensions are also discussed. Some of the important methods to treat these problems and challenges are presented. Characteristic numerical and experimental results are discussed for a few important areas. The implications of such results in improving practical systems and processes, including enhanced process feasibility and product quality, are also discussed. [DOI: 10.1115/1.3056576]

1 Introduction

Microscale thermal transport processes are particularly important in materials processing, which is presently one of the most active areas of research in heat transfer. We have seen substantial growth and development of new advanced materials and processing methods to meet the critical demand for special material properties in a variety of new and emerging applications that arise in energy, bioengineering, transportation, communications, computers, and other fields. Many of the relevant devices and systems are in the microscale range due to the dimensions involved. Also, the quality and characteristics of the final product resulting from materials processing are strongly dependent on the transport processes that arise at microscale, or nanoscale, levels. Due to growing international competition and stringent demands placed on devices, sensors, and equipment, it is has become critical to improve the quality and characteristics of the product, while optimizing the processing techniques and the manufacturing systems involved.

Fluid flow and the associated heat and mass transfer are extremely important in the thermal processing of materials, which refers to manufacturing and material fabrication techniques that are strongly dependent on the thermal transport mechanisms. With the growing interest in new and advanced materials such as composites, ceramics, polymers, glass, coatings, specialized alloys, and semiconductor materials, thermal processing has become particularly important since the properties and characteristics of the product can be largely controlled by thermal transport mechanisms, as discussed by Jaluria [1,2]. Besides the traditional processes, such as welding, metal forming, polymer extrusion, casting, heat treatment, and drying, thermal processing includes new and emerging methods, such as crystal growing, chemical vapor deposition, thermal sprays, fabrication of composite materials, processing of nanopowders to fabricate system components, optical fiber drawing and coating, microgravity materials processing, laser machining, and reactive extrusion.

A few of these processes, in which microscale transport phenomena are of particular importance in determining the quality and characteristics of the device or item being fabricated, are shown in Fig. 1. These include thin film fabrication by chemical vapor deposition (CVD), the optical glass fiber drawing process in which a specially fabricated glass preform is heated, drawn, cooled, and coated into a fiber, and Czochralski crystal growing in which molten material such as silicon is allowed to solidify across an interface as a seed of pure crystal is withdrawn. In all these processes, the quality and characteristics of the final product and the rate of fabrication are strong functions of the underlying microscale thermal transport processes; see, for instance, Refs. [3–6]. For example, the flows that arise in the molten material in crystal growing due to temperature and concentration differences affect the quality of the crystal and, thus, of the semiconductors fabricated from the crystal. Also, the microstructure of the crystal is determined by the micro- and nanoscale processes occurring at the solid-liquid interface. It is important to understand these flows and develop methods to minimize or control their effects. Similarly, the profile of the neck-down region in an optical fiber drawing process is governed by the viscous flow of molten glass, which is in turn determined by the thermal field in the glass. Thermally induced defects arise due to the breaking of the Si–O bonds, microcracks result from the tension, and other defects are caused by local instabilities. Microscale transport of dopants added to the material in order to enhance or modify the optical behavior of the fiber is also important in the determination of the characteristics of the fiber obtained. The buoyancy-driven flows generated in the liquid melt in casting processes strongly influence the microstructure of the casting and the shape, movement, and other characteristics of the solid-liquid interface. In chemical vapor deposition, the heat and mass transfer processes occurring at

---

Contributed by the Heat Transfer Division of ASME for publication in the JOURNAL OF HEAT TRANSFER. Manuscript received August 3, 2008; final manuscript received September 27, 2008; published online January 26, 2009. Review conducted by Robert D. Tzou.

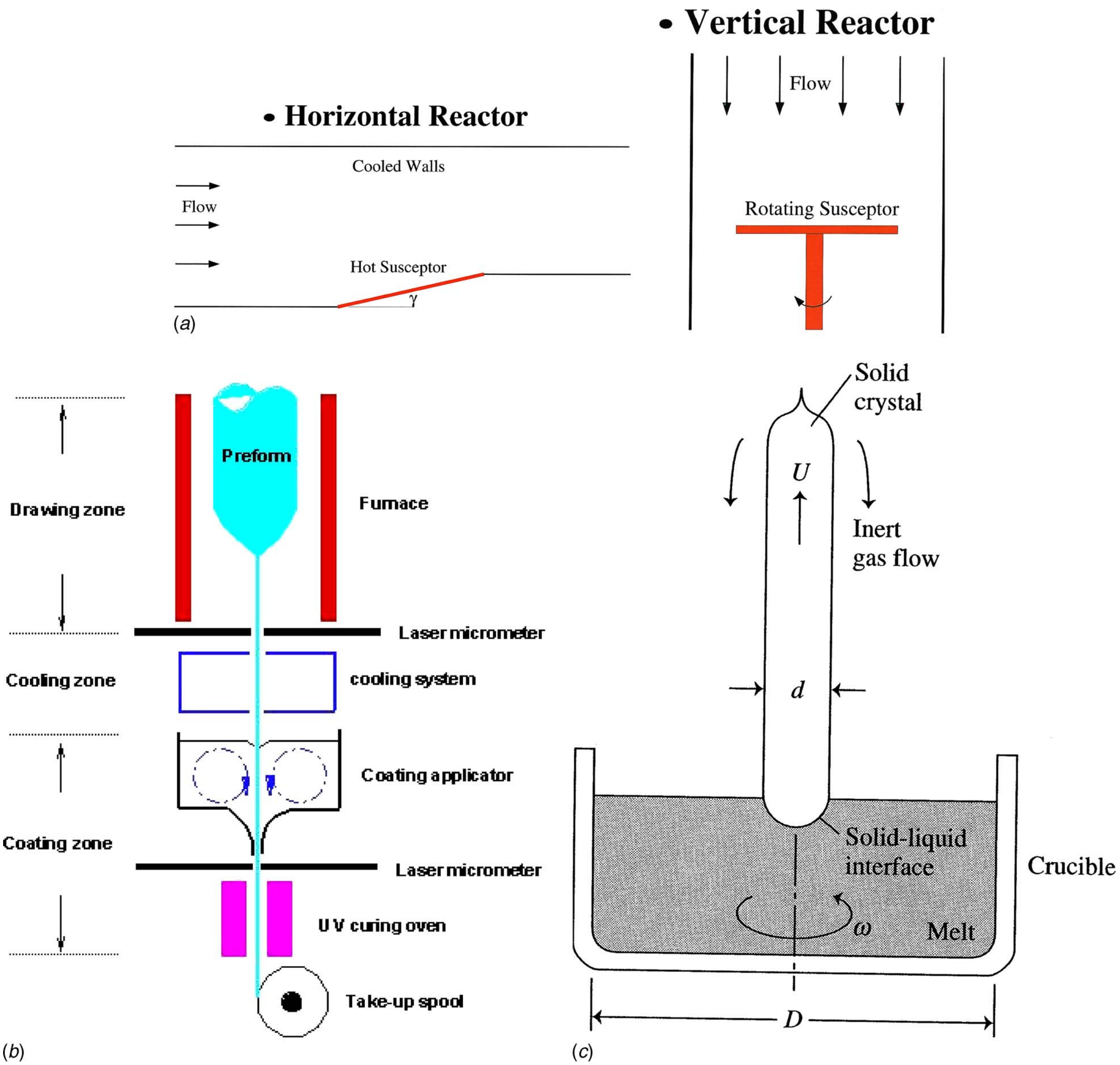

Fig. 1 Sketches of a few thermal materials processing applications that involve microscale transport phenomena. (*a*) Chemical vapor deposition. (*b*) Optical fiber drawing. (*c*) Czochralski crystal growing.

micro- and nanometer dimensions determine the deposition rate, uniformity, and the overall quality of the thin film produced.

Another important aspect is the link between the microscale transport and the materials processing systems, which involve macroscale or commercial scale considerations. An understanding of the microscale mechanisms that determine material characteristics is important, but these must be linked with the boundary conditions that are usually imposed at the macroscale level in the thermal materials processing system, as is evident from the systems shown in Fig. 1.

This review paper is directed at these important issues, focusing on microscale transport in thermal processing of materials and linking these with the characteristics of the product and with the system. A range of processes is considered in order to discuss the important basic considerations that arise in microscale devices, experimental and analytical/numerical approaches to deal with the microscale transport mechanisms, and their effect on the processed material. As mentioned above, the two main aspects that are considered in this paper are as follows:

1. applications and devices at microscale dimensions
2. microscale mechanisms that determine material characteristics during processing

Thus, the paper first focuses on microscale devices and discusses the major basic concerns and challenges that arise at these dimensions, which typically range from a few microns to around 200 μm. These include, for instance, numerical modeling with very fine grids, strong viscous dissipation effects, high pressures needed for the flow, experimentation over micrometer scales, applicability of traditional analyses, and mechanisms, such as surface tension, that could increase in significance as the dimensions are reduced. The paper next discusses the considerations related to underlying microscale mechanisms in materials processing and their effects on the quality of the device or product being fabricated. Examples include thermally induced defects, material conversion due to shear and temperature, chemical reactions leading to deposition, and microstructure changes as the material undergoes processing. The link between these aspects and the quality

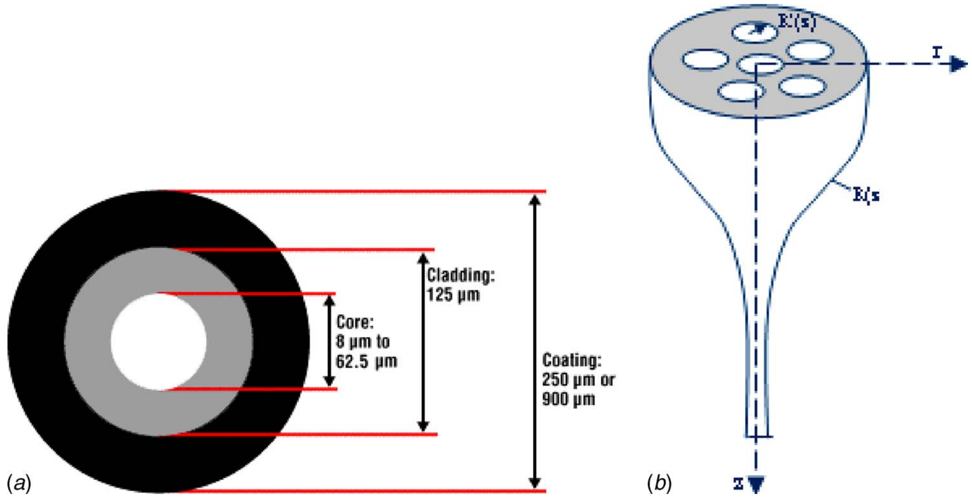

Fig. 2 (*a*) Structure of a typical optical fiber; (*b*) sketch of a microstructured optical fiber

and characteristics of the product, rate of production, cost, process feasibility, and process optimization are also discussed.

2 Applications and Devices at Microscale Dimensions

As mentioned earlier, the flow and heat transfer at micrometer dimensions are of interest in many thermal materials processing applications. Because of the small dimensions, the major concerns that arise are high-pressure differences, significant viscous dissipation, difficulty in measurements, particularly near the surfaces, and analytical/numerical modeling. However, if the problem involves dimensions that are much larger than the mean free path of the molecules, no-slip conditions at the walls and continuity can be assumed, resulting in modeling, which is similar to modeling at the macroscale.

For telecommunication purposes, the optical fiber usually consists of three components, core, cladding, and coating, as shown in Fig. 2(*a*) for the so-called "weakly guiding fiber." In this multilayered structure, the light-guiding central portion, or core, is covered by a dielectric layer, or cladding, which generally has a refractive index lower than that of the core to obtain total internal reflection in the core. In practice, core sizes vary from 8.3 μm to 62.5 μm. Radiation heat transfer is the dominant mode of transport in the heating process and the viscosity of the glass, which is a subcooled liquid, affects the flow and the draw tension, which in turn affects the transmission properties and also results in strength degradation [7]. Coating of the fiber with a jacketing material is carried out for protection against abrasion and for increased strength. Again, the coating thickness is in microns and defects in the coating are important for the quality of the final optical properties of the fiber. Interest in hollow or microstructure fibers, which form an important class of optical fibers, has grown recently since these fibers have many advantages over the conventional solid-core optical fibers. These include high laser power thresholds, low insertion loss, no end reflection, ruggedness, and small beam divergence. Due to the presence of the air core, microstructure fibers can achieve a low attenuation through structural design rather than high-transparency material selection and can be used to provide infrared laser beam and the high-power delivery [8]. Microstructure optical fibers are widely used for medical applications, sensor technology, diagnostics, and CO_2 and laser delivery, besides traditional telecommunications [9]. Figure 2(*b*) shows a sketch of a microstructured fiber, with several microchannels that contain air or inert gases and that are typically 10–20 μm in diameter. The typical dimensions that are of interest in these and other such applications are given in Table 1.

2.1 Furnace Drawing of Optical Fibers. The manufacture of an optical fiber typically begins with a silica preform, which generally consists of two concentric cylinders called the core and the cladding and which may be doped with various elements or chemicals to achieve desired optical properties. In a draw tower, the preform is traversed vertically through a high-temperature cylindrical furnace. The glass is heated beyond its softening point T_{melt} of about 1900 K for silica and is drawn into a fiber of diameter around 125 μm by applying axial tension. Studies on pure, single-layer, solid, silica optical fiber drawing have been carried out by a number of researchers. Paek and Runk [10] studied the neck-down profile and temperature distribution within the neck-down region using a one-dimensional analysis. Myers [11] developed a one-dimensional model for unsteady glass flow. More comprehensive models have been developed by Jaluria and coworkers [12–15]. They investigated the flow and the thermal transport in detail, including the convective and radiative heat transfer in the axisymmetric configuration of the glass preform and the inert gas flow. An analytical/numerical method was developed to generate the neck-down profile. The effects of fiber draw speed, inert gas velocity, furnace dimensions and furnace temperature distribution on the flow, temperature distribution, tension, and neck-down shape were obtained and discussed. Initially, the preform was assumed to be optically thick, which is not valid in the

Table 1 Typical dimensions of some microscale devices and applications

Solid optical fibers
Single mode: 5–10 μm
Multimode: 10–50 μm

Coatings
Primary coating: 30–50 μm
Secondary coating: 50–100 μm

Hollow fibers
Hole diameter: 10–50 μm
Multistructured: Hole diameter 5–10 μm

Chemical vapor deposition
Coatings: 1–10 μm
Films: 10–50 μm

Chemical conversion, defect generation
Submicron scale (micro- and nanoscale)

lower neck-down region and which was later modeled with the zonal method. High-speed optical fiber drawing, up to 20 m/s, with preform diameters of 5–10 cm was investigated. More recently, Wei et al. [16] used the discrete ordinate method to solve the radiative transfer equation and numerical results for higher-speed (25 m/s) drawing were obtained. However, the major constraint has been the availability of accurate radiative property data.

The flow of the glass and of the aiding purge gas in a cylindrical furnace is assumed to be axisymmentric. The governing equations for the glass and the gas are given as

$$\frac{\partial v}{\partial z}+\frac{1}{r}\frac{\partial (ru)}{\partial r}=0 \tag{1}$$

$$\frac{\partial v}{\partial t}+u\frac{\partial v}{\partial r}+v\frac{\partial v}{\partial z}=-\frac{1}{\rho}\frac{\partial p}{\partial z}+\frac{1}{r}\frac{\partial}{\partial r}\left[r\upsilon\left(\frac{\partial v}{\partial r}+\frac{\partial u}{\partial z}\right)\right]+2\frac{\partial}{\partial z}\left(\upsilon\frac{\partial v}{\partial z}\right) \tag{2}$$

$$\frac{\partial u}{\partial t}+u\frac{\partial u}{\partial r}+v\frac{\partial u}{\partial z}=-\frac{1}{\rho}\frac{\partial p}{\partial r}+\frac{2}{r}\frac{\partial}{\partial r}\left(r\upsilon\frac{\partial u}{\partial r}\right)+\frac{\partial}{\partial z}\left[\upsilon\left(\frac{\partial v}{\partial r}+\frac{\partial u}{\partial z}\right)\right]-\frac{2\upsilon u}{r^2} \tag{3}$$

$$\rho C_p\left(\frac{\partial T}{\partial t}+u\frac{\partial T}{\partial r}+v\frac{\partial T}{\partial z}\right)=\frac{1}{r}\frac{\partial}{\partial r}\left(rK\frac{\partial T}{\partial r}\right)+\frac{\partial}{\partial z}\left(K\frac{\partial T}{\partial z}\right)+\Phi+S_r \tag{4}$$

where Φ is the viscous dissipation term and S_r is the radiation source term. The other variables are defined in the Nomenclature.

For glass, the material properties are strong functions of the temperature T. They also vary with composition and changes in the microstructure, the main effect being on the radiation properties and on the refractive index. The variation in the viscosity is the most critical one for the flow, since it varies quite dramatically with temperature. An equation based on the curve fit of available data for kinematic viscosity υ is written for silica, in SI units, as

$$\upsilon=4545.45\exp\left[32\left(\frac{T_{\text{melt}}}{T}-1\right)\right] \tag{5}$$

indicating the strong exponential variation of υ with temperature. Variations in all the other relevant properties of glass need to be considered as well, even though the variation with T is not as strong as that of viscosity. The properties of the purge gas in the furnace may be considered to be constant since their variations are small over the temperature ranges encountered. The radiative source term S_r in Eq. (4) is nonzero for the glass preform/fiber because glass emits and absorbs energy. The variation of the absorption coefficient with wavelength λ can often be approximated in terms of bands with constant absorption over each band. A two- or three-band absorption coefficient distribution has been effectively used. One of the methods that have been used successfully to model the radiative transport is the zonal model. Figure 3 shows the typical finite volume zones used for radiative transfer. Because of the small fiber diameter, being around 125 μm, there is a temptation to assume uniform temperature across the fiber. However, because of the high-temperature dependence of the viscosity, this assumption does not yield accurate results and a large number of grid points, typically around 50, are needed across the fiber radius of around 62.5 μm to capture changes in temperature and the consequent effects on properties, viscous dissipation, thermally induced defects, and dopant movement.

Figures 4 and 5 show some typical results obtained from the numerical simulation. The fiber drawing process involves modeling the free surface flow of glass. A solution of the transport equations, along with a surface force balance, is needed for the determination of the neck-down profile. The normal force balance and the vertical momentum equations are used to obtain a correction scheme for the neck-down profile and the iterative process is continued until the neck-down shape does not change from one iteration to the next. It was found that viscous and gravitational forces are dominant in the determination of the profile. Surface tension effects are small, despite the small dimensions involved. For convergent cases, perturbations to the initial profile and different starting shapes lead to the converged neck-down profile, indicating the robustness of the scheme and the stability of the drawing process, as seen in Fig. 4(*a*).The force balance conditions are also closely satisfied if the iterations converge [14]. However, as expected, it is not possible to draw the fiber under all imposed conditions. If the furnace temperature is not high enough, it is found that the fiber breaks due to lack of material flow, a phenomenon that is known as viscous rupture. This is first indicated by the divergence of the numerical correction scheme for the profile and is then confirmed by excessive tension in the fiber. Similarly, it is determined that, for a given furnace temperature, there is a limit on the draw speed beyond which drawing is not possible, as this leads to rupture. A region in which drawing is feasible can be identified, as shown in Fig. 4(*b*). Beyond the boundaries of this region, drawing is not possible. Similarly, different combinations of other physical and process variables, such as the inert gas flow velocity, flow configuration, furnace wall temperature distribution, furnace length and diameter, and preform and fiber diameters, may be considered to determine the feasibility of the process [17].

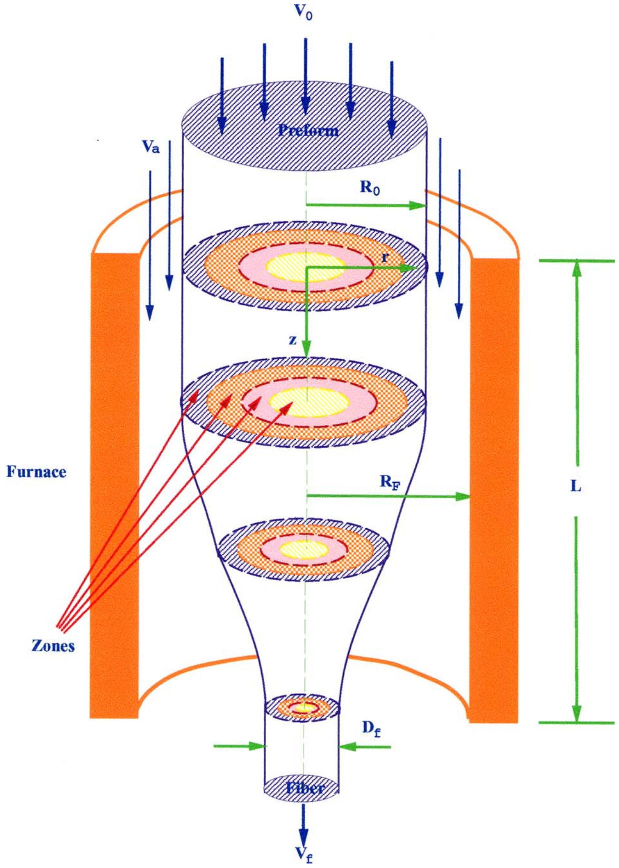

Fig. 3 Axisymmetric finite volume zones for the calculation of radiation in the glass preform and fiber

Typical computed results in the neck-down region are shown in Fig. 5 in terms of the temperature distribution and the viscous dissipation. The flow was found to be smooth and well layered because of the high viscosity. Typical temperature differences of 50–100°C arise across the fiber. Viscous dissipation, though relatively small compared with the total energy transport, is mainly concentrated near the end of the neck-down, in the microscale

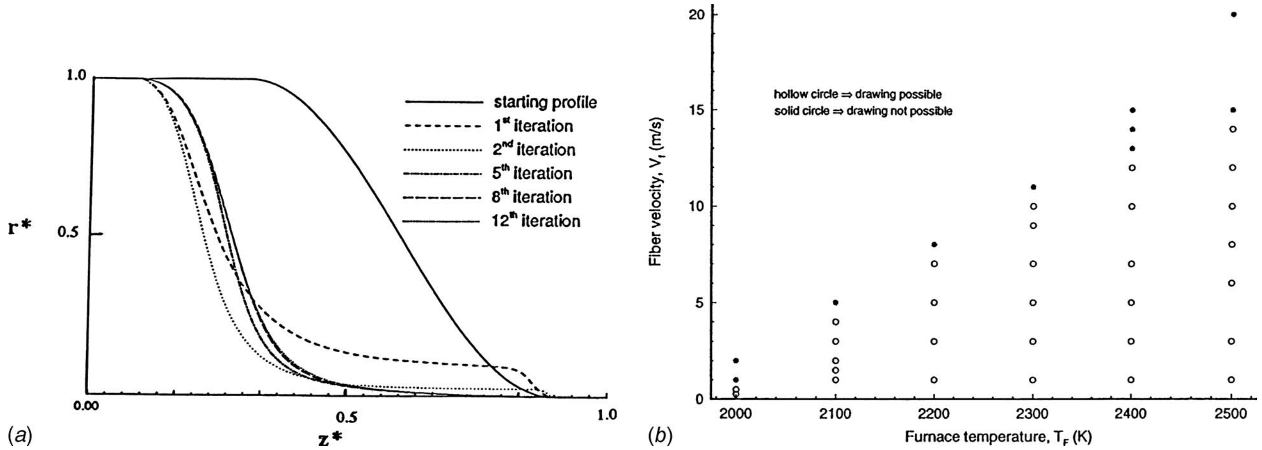

Fig. 4 (*a*) Iterative convergence of the neck-down profile in optical fiber drawing. Here, $r^* = r/R$ and $z^* = z/L$, where R is the preform radius and L is the furnace length; (*b*) feasibility of the optical fiber drawing process, as indicated by regions where drawing is not possible due to viscous rupture resulting from excessive draw tension.

region, and plays an important role in maintaining the temperatures above the softening point. Figure 6 shows a comparison with experimental results on the neck-down profile and thus lends support to the modeling of the process. However, experiments are considerably complicated due to the small dimensions of the fiber, high temperatures in the draw furnace, and large draw speeds. Such experimental results are fairly difficult and are obtained on the draw tower by stopping the draw process and studying the drawdown shape of the preform [18].

2.2 Multilayer and Hollow Fibers. As mentioned earlier, for telecommunication purposes, the optical fiber usually consists of the core and the cladding, with standard core sizes in use today being 8.3 μm, 50 μm, and 62.5 μm, and the diameter of the cladding surrounding each of these cores being around 125 μm [10,18]. The core-cladding structure may be treated as different fluids with different properties. Separate body-fitted grids are applied to the different layers and to the inert gas. Each separate layer in the glass is assumed to have a uniform refractive index, bounded by diffuse surfaces. The zonal method is applied to calculate the radiation transfer inside the three enclosures, as developed by Chen and Jaluria [19]. The two-band model presented by Myers [11] for the absorption coefficient a of pure silica was used. This is given by the equations

$$a = 0 \quad \text{for} \quad \lambda < 3.0\ \mu\text{m} \tag{6}$$

$$a = 400.0\ \text{m}^{-1} \quad \text{for} \quad 3.0\ \mu\text{m} \le \lambda < 4.8\ \mu\text{m} \tag{7}$$

$$a = 15{,}000\ \text{m}^{-1} \quad \text{for} \quad 4.8\ \mu\text{m} \le \lambda < 8.0\ \mu\text{m} \tag{8}$$

Figure 7(*a*) shows a typical mesh for the two-layer optical fiber drawing process. The preform typically goes from a diameter of around 10 cm to the fiber diameter of 125 μm in a distance of around 0.3 m. Thus, extra care has to be exercised near the bottom of the region to avoid highly distorted grids due to the small diameter of the fiber. The optimal grid can be obtained by numerical experimentation. The core is shown as half in diameter as the cladding. However, it can be much smaller in diameter for single-mode telecommunication applications, being as small as around 8 μm. Again, it is not accurate to assume uniform temperature and velocity in the core, despite the small dimension, because of the large changes in viscosity due to temperature differences. The boundary conditions of shear, pressure, velocity, and temperature continuity have to be satisfied at the interface between the two layers. A typical example of the numerically calculated neck-down profile for a two-layer optical fiber is shown in Fig. 7(*b*). The force balance conditions are checked at all the interfaces and the radiation calculations are much more involved than for a single-layer fiber discussed earlier.

When the core and the cladding are doped with various dopants, the refractive index and absorption coefficients are affected [20]. Since radiation heat transfer is the dominant mode of transport in the heating process, a nonuniform distribution of radiation properties in the preform due to this microscale doping will cause significant local effects and will thus affect the draw process. Assumed magnitudes of change in the refractive index and absorption coefficients were used by Chen [21] to capture the generic effects of variation in these two properties. The core is taken as pure fused silica and the cladding is doped.

GeO_2 is mainly used as a dopant for the core to increase the refractive index, which will also increase the ultraviolet radiation absorption and lower the viscosity. In this study, the core is doped with 5.5 mol %, 11.1 mol %, and 16.6 mol % GeO_2, respectively, to obtain relative refractive index differences of 0.5%, 1.0%, and 1.5% in the fiber. In Fig. 8(*a*), the isotherms for various GeO_2 concentrations are shown with a reference profile to demonstrate the variations in temperature levels in the axial direction. It is seen that, when the core is doped with GeO_2, the core is heated up to the same temperature level in a shorter distance than the cladding. The distance to reach a certain temperature level for the whole preform decreases with increasing GeO_2 concentration. The reason is that, since GeO_2-doped silica core has a larger radiation coefficient in the ultraviolet region and the transmissivity of pure silica cladding is very high in this region, the GeO_2-doped silica core absorbs more energy by radiation than pure silica core. Figure 8(*b*) shows the temperature of the preform along the centerline for pure silica and GeO_2-doped silica core with a pure silica cladding, for various GeO_2 concentrations. As expected, a significant increase in the centerline temperature is observed in the upper neck-down region with greater GeO_2 doping. Beyond that, the fiber with a higher GeO_2 concentration maintains a slightly higher temperature along the centerline. Several other results are given by Chen [21].

Similar considerations arise for the drawing of a hollow fiber, where the hollow core is a microchannel of diameter 40–80 μm. Some characteristic results are given here. The furnace diameter is taken as 7 cm and its length is 30 cm. The inner and outer diameters of the preform are 2.5 cm and 5 cm, respectively. The furnace temperature is assumed to be a parabolic profile with a maximum of 2500 K in the middle and a minimum of 2000 K at the two ends. The fiber drawing speed is 10 m/s. The velocity of the

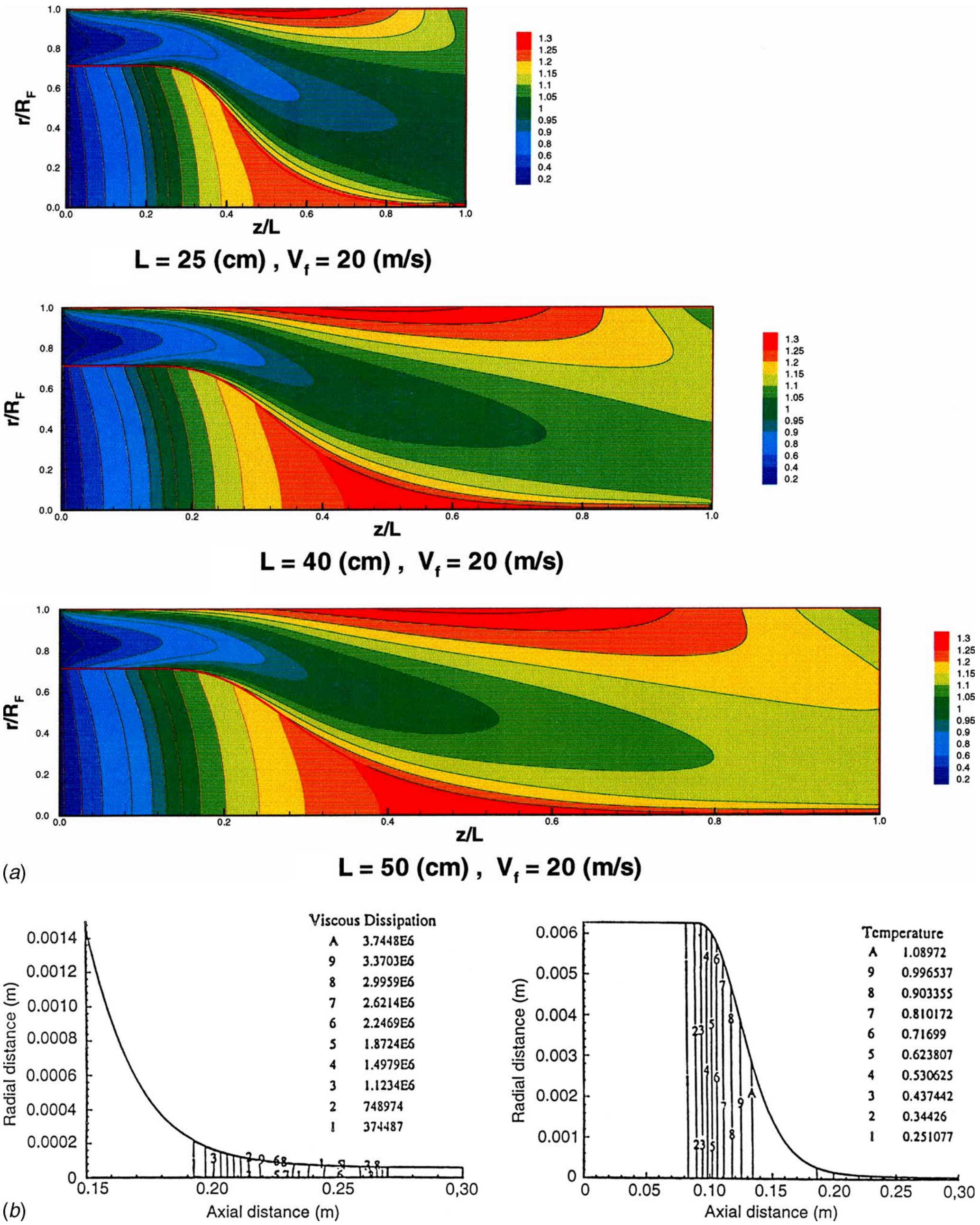

Fig. 5 (***a***) **Calculated temperature field in the glass during drawing of a single-layer optical fiber for three furnace lengths; (*b*) calculated viscous dissipation and temperature contours in the optical fiber drawing process for typical drawing conditions**

purge gas at the inlet is 0.1 m/s. Pressurization of the gas in the core is neglected. The results in terms of streamlines and isotherms are shown in Fig. 9. The thicker black lines indicate the two neck-down profiles. The isotherms are in terms of the nondimensional temperature, with the softening temperature as the characteristic temperature. It is clear that the flow and temperature distributions in the fiber and in the external gas in hollow fiber drawing are similar to those in the solid-core fiber drawing. Because of the thinness of the central core, the air in the core is dragged by the moving fiber. A slug flow approximation is made for the airflow to simplify the analysis. The magnitude of the velocity of the natural convection flow is so small that thermal diffusion dominates in the central cavity.

A collapse ratio C is defined to describe the collapse process of the central microchannel as

$$C(z) = 1 - (R_1(z)/R_2(z))/(R_{10}/R_{20}) \tag{9}$$

Thus, $C=0$ when the radius ratio of the final fiber equals the initial radius ratio, and $C=1$ when the central cavity is closed. The effects of the perform feeding and fiber drawing speeds and the furnace temperature on collapse ratio are studied. The variation of the collapse ratio with the axial distance for different feeding and drawing speeds and for different furnace temperatures is shown in Fig. 10(*a*). It is seen that the collapse ratio increases along the axis and increases with a decrease in drawing speed or a decrease in feeding speed. The effect of preform feed rate on the collapse ratio is much larger than that of the fiber drawing speed. The collapse ratio increases at larger furnace temperature. All these trends are similar to the results from Chakravarthy and Chiu [22]. These phenomena can be explained by using the "collapse time" of

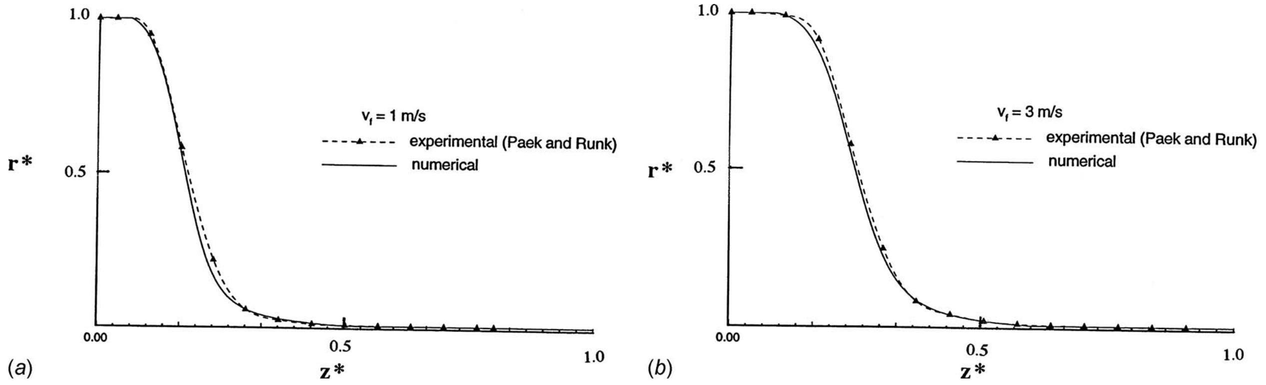

Fig. 6 Comparison of the numerical predictions of the neck-down profile with experimental results

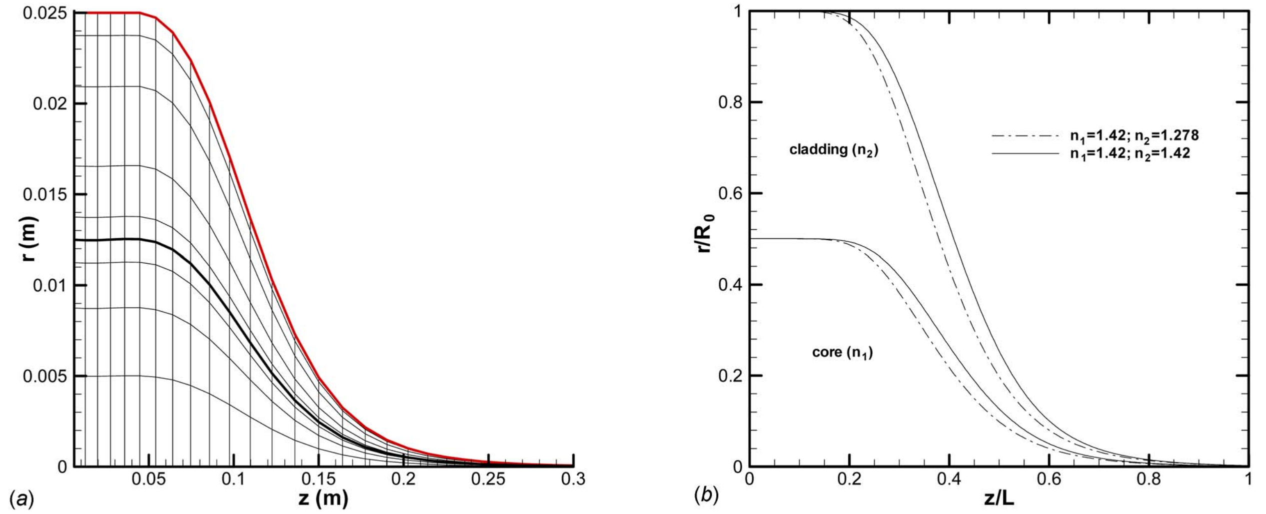

Fig. 7 Numerical grid and calculated neck-down profiles for a preform with a core-cladding structure at two values of the refractive index of the outer layer

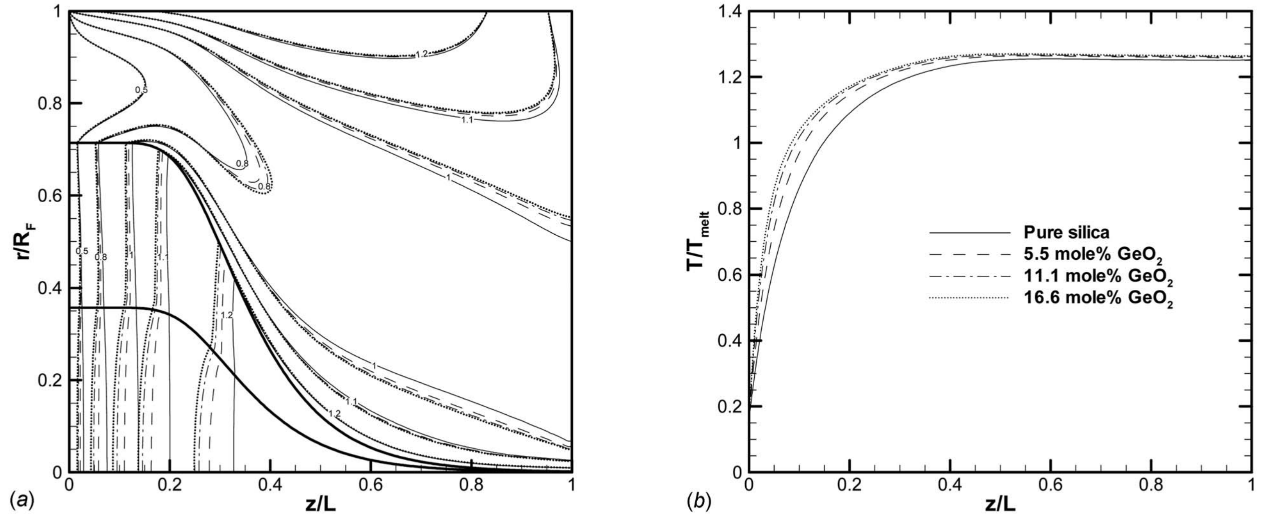

Fig. 8 (*a*) Isotherms for various GeO_2 concentrations (solid line: pure silica; dashed line: 5.5 mol % GeO_2; dashed dotted line: 11.1 mol % GeO_2; dotted line: 16.6 mol % GeO_2); (*b*) temperature variation along the centerline for various GeO_2 concentrations

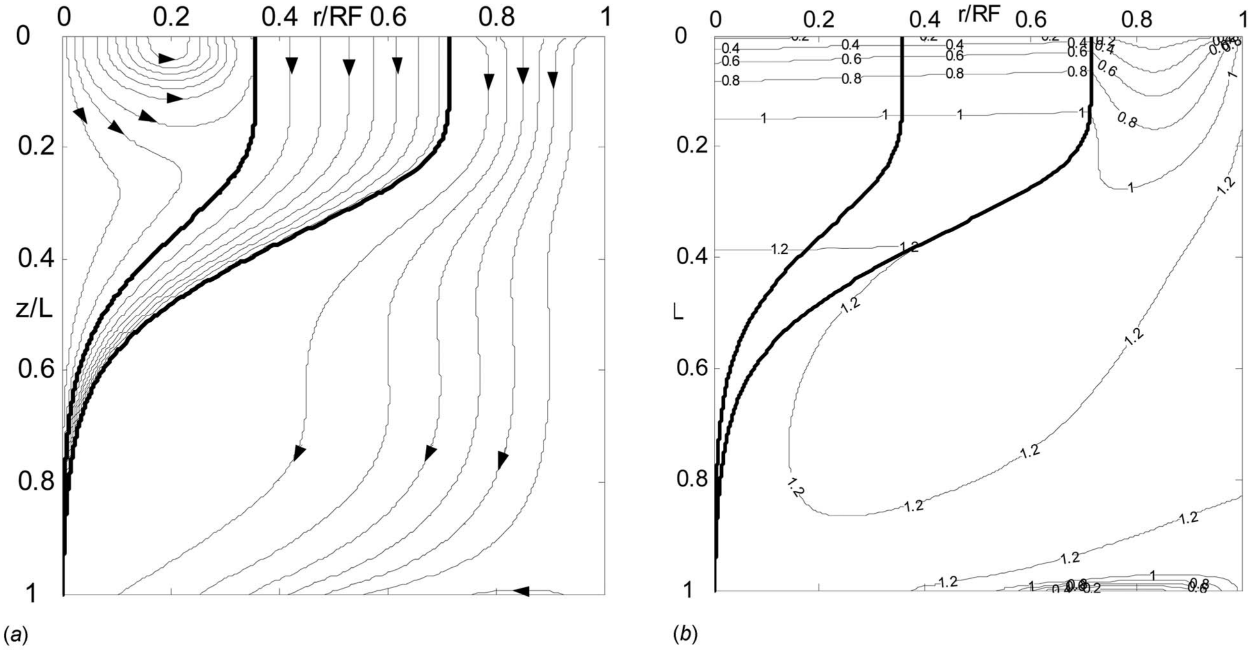

Fig. 9 Streamlines and isotherms in the furnace for a typical case of hollow fiber drawing with a parabolic furnace temperature distribution at a drawing speed of 10 m/s

preform/fiber in the drawing furnace. When the drawing or feeding speed decreases, the total time of preform/fiber in the furnace increases. The total time of preform/fiber in the furnace is comprised of the time to heat the preform up to the softening temperature and the time for the preform/fiber to collapse. The collapse time increases since the time to heat the preform is nearly the same for different drawing or feeding speeds. Therefore, the collapse ratio increases due to an increase in the collapse time when the drawing or feeding speed decreases. Since the drawing speed is much higher than the feeding speed, the collapse time is more sensitive to the feeding speed than the drawing speed. Also the time to heat the preform is shorter at higher furnace temperature, which implies the collapse time increases at given feeding and drawing speeds. Hence, the collapse ratio increases at higher furnace temperature, as seen in Fig. 10(*b*). In order to avoid the collapse of the central cavity, we can increase the drawing and feeding speeds, decrease the furnace temperature, or increase the preform radius ratio. The collapse ratio is also influenced by the pressure difference between the purge gas and the central cavity. It was shown that the collapse ratio decreases with a decrease in the pressure difference. This is because higher pressure in the central cavity tends to prevent collapse of the central cavity [23]. It was also seen that high negative pressure difference may cause the central cavity to enlarge during the drawing process. This is called "explosion" in the drawing process. Because of the size of the core, surface tension is an important parameter and plays a very significant role in the collapse.

The hollow fiber cannot be drawn at any arbitrary combination of critical drawing parameters, as seen earlier for solid-core fibers. Figure 11(*a*) shows an infeasible case, which arises due to the lack of material flow. It is seen that the neck-down profiles become quite flat after 12 iterations. This phenomenon is similar to that seen in the solid-core fiber drawing process [14]. Figure 11(*b*) illustrates the feasible domain in terms of drawing temperature and drawing speed. Drawing speed is in the range 1–20 m/s. It shows that drawing process is possible only in the region between

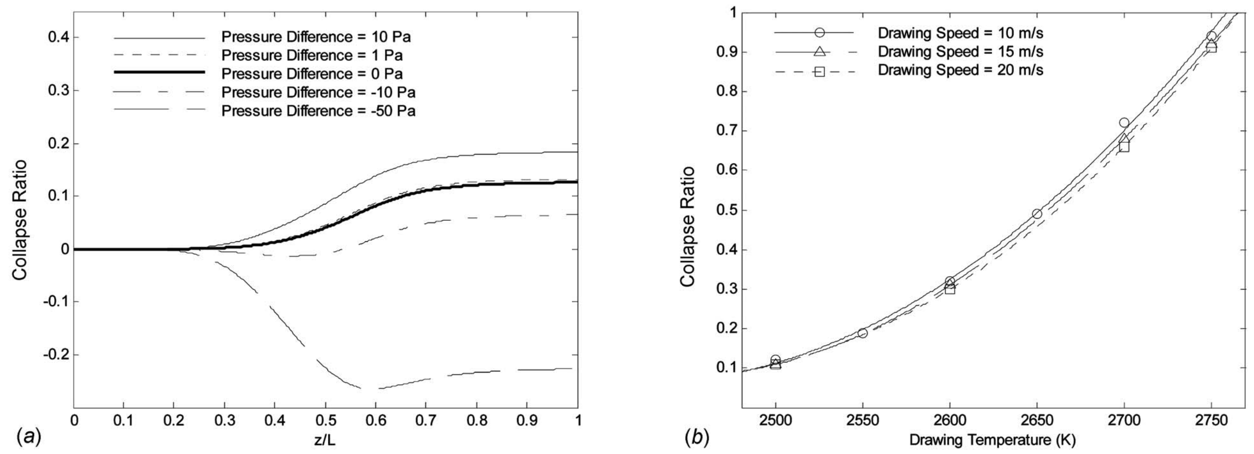

Fig. 10 (*a*) Variation of collapse ratio along the axis with different pressurizations in the core and (*b*) with the drawing temperature for different drawing speeds

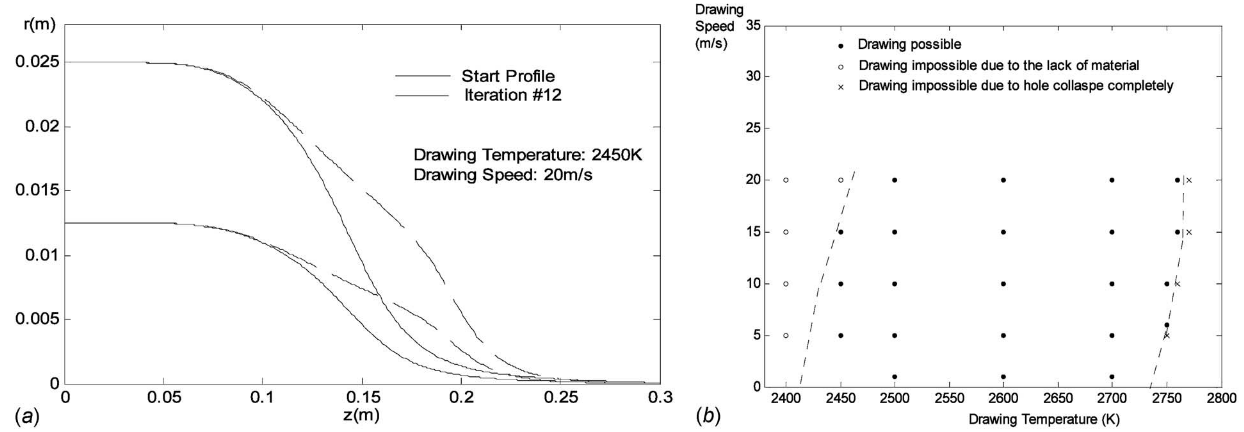

Fig. 11 (*a*) **Neck-down profile corrections for an infeasible drawing case; (*b*) feasible domain for hollow fiber drawing in terms of the drawing speed and the drawing temperature**

two dashed lines. The left boundary exists because the continuous drawing process may fail due to the lack of material flow at low furnace temperature or high drawing speeds, which is initially indicated by the divergence of the numerical correction scheme for the profiles. The right boundary exists only for hollow optical fiber because high furnace temperature or low drawing speeds may cause the central air core to collapse completely. At the right side of this boundary line, the central air core is closed during the drawing process. Therefore, there are two thresholds for the drawing temperature at the same drawing speed. These two boundary lines are nearly vertical since the effect of the drawing speed is relatively weak, which has been indicated by the earlier parameter study [23].

2.3 Fiber Coating. Optical fibers are coated with a jacketing material for protection against abrasion, to increase strength, and to reduce stress-induced microbending losses. Typical coating thicknesses are of the order of 40–50 μm and are applied to the uncoated fiber or as secondary coating to a coated fiber. The basic coating process involves drawing the fiber of diameter around 125 μm through a reservoir of coating fluid, with inlet and outlet dies. This is immediately followed by a curing process of the polymer coating material around the fiber. Figure 12(*a*) shows a schematic of a typical coating applicator and die system. Though the chamber is 1–2 cm in diameter, the entrance and exit dies are channels with diameters to yield gap thickness between the moving fiber and the die wall of 50–100 μm. Viscous shear due to the moving fiber results in a circulatory fluid motion within the fluid. A balance between surface tension, viscous, gravitational, and pressure forces results in an upstream meniscus at the cup entrance, as shown in Fig. 12(*b*). A downstream meniscus at the die exit results again from a balance of viscous, gravitational, and inertia forces, along with the surface tension forces. Centering forces within the tapered die contribute to the positioning of the fiber at the die exit center. Successful coatings are concentric, of uniform thickness, and free of particle inclusions or bubbles [24].

Under ideal operating conditions, at the entrance die, the coating liquid in the vicinity of a dynamic contact surface, which forms an upstream meniscus between the air, the liquid, and the moving fiber, replaces the air entrained with the moving fiber. However, at high speeds, the meniscus breaks down, with "sawtooth" instability, as shown in Fig. 12(*b*), and air entrained into the coating. The use of high draw rates requires consideration of alternate pressurized applicator designs, where pressure induced motion of the coating material is used to reduce the shear at the fiber surface and helps in the establishment of a stable free surface flow. An additional benefit resulting with such pressurized dies has been the incorporation of gas bubble reducing, or bubble stripping, designs, which have resulted in minimizing gas bubbles entrained at the coating cup entrance and then trapped within the coating layer.

At the die exit, the coating material is drawn out with the fiber, forming a downstream meniscus, whose shape is primarily deter-

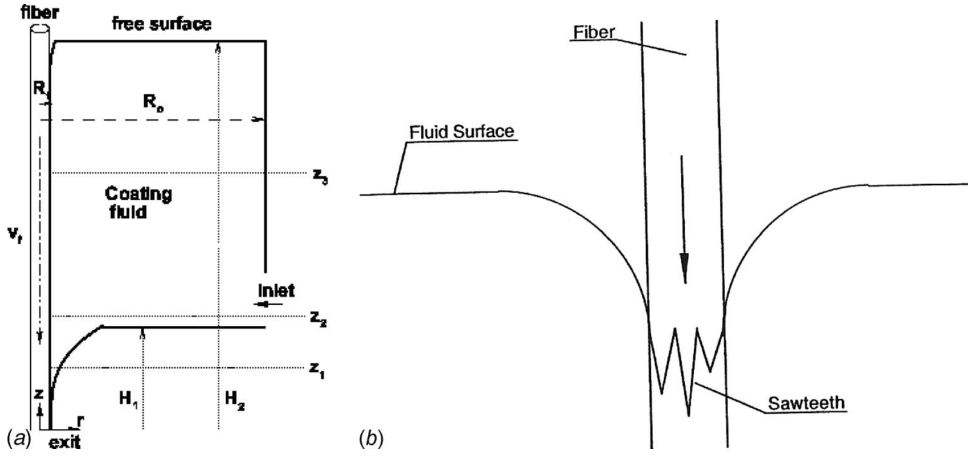

Fig. 12 (*a*) **A typical optical fiber coating applicator; (*b*) instability and breakdown of the entrance meniscus in the microchannel inlet at high speeds**

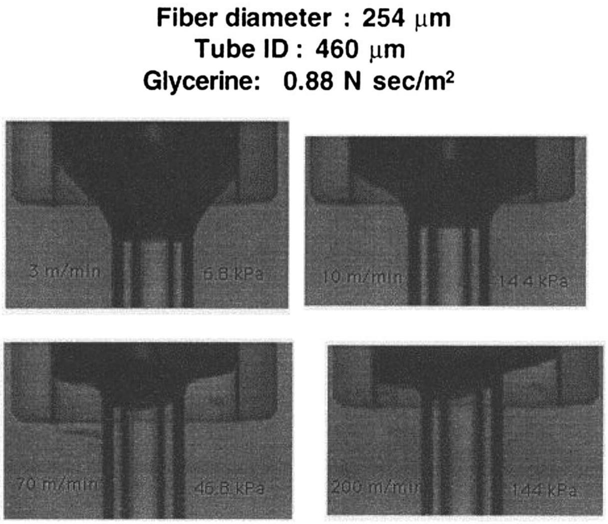

Fig. 13 Entrance flow in the microchannel inlet of annular gap thickness 103 μm at different pressures and draw speeds

mined by a balance between viscous, gravitational, and inertia forces. The control of the coating characteristics is of major concern in the industry. These considerations have become particularly important as the coating speeds have been increased to values beyond 20 m/s to enhance productivity and as the interest in specialty fibers and fibers of different materials, including polymer fibers, has grown. The physical properties of the polymer coating materials, particularly the viscosity, and their dependence on temperature are of primary importance in the coating process. Surface tension has a significant effect on the flow near the free surface, which represents the interface between liquid and gas in many cases, and on the shape, stability, and other characteristics of the interface. Surface tension affects the force balance on a free surface and affects the equilibrium shape of the interface. For typical optical fiber dimensions, the diameter being of order 125 μm, surface tension effects are often very large and gravitational effects are often small. However, for larger dimensions, particularly for plates and cylinders of diameter in centimeters, gravity could dominate over surface tension and over several other forces.

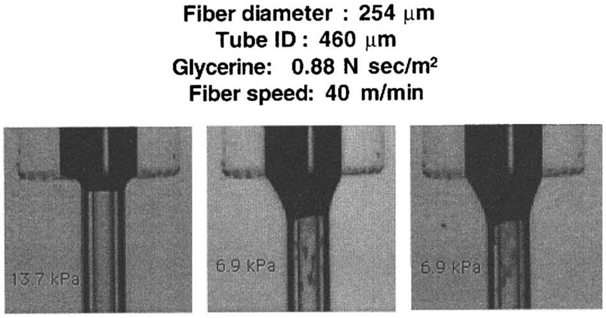

Fig. 14 Meniscus for different imposed pressures, showing breakdown at low pressure

A few typical results from these studies are discussed here. The experimental work has been carried out on a fiber coating facility to study the upstream and downstream menisci, with glycerin/water solutions as test fluids. Glycerin is convenient for such studies because its viscosity at 20°C is in the range 1 N s/m^2, which is similar to that used in coating applications. The microchannels that form the inlet and exit dies can be changed so that different geometries and diameters can be investigated [25].

Figures 13 and 14 show images of the meniscus formed with the fiber moving through the micropipette inlet tube into the applicator. The fiber speed ranges from 3 m/min to 200 m/min. Different diameters and imposed pressures are employed. Figure 14(*c*) clearly shows the breakdown of the meniscus into sawtooth patterns and tip streaming as previously mentioned. On the other hand, at higher imposed pressures, the meniscus image appears to be smooth, suggesting suppression of large-scale breakdown at the same fiber speed. The unpressurized meniscus generates a large number of relatively large air bubbles compared with the pressurized meniscus. A comparison of the shape of the menisci in the figures shows that the effect of the imposed pressure is to flatten the meniscus and to increase the slope of the liquid-air interface near the fiber compared with that for an unpressurized meniscus. This results in a smaller air volume available for entrainment, accounting for the difference between the figures. The effect of the imposed pressure on the meniscus shape for a fiber moving in a tube is also seen, indicating the flattening of the profile as well as an upward movement of the meniscus as the pressure increases. These results are summarized in Fig. 15. The first part gives the fiber speed for breakdown as a function of the applicator pressure, indicating higher speeds before breakdown occurs at larger pressure. Figure 15(*b*) shows the dependence of the location of the meniscus in the microchannel, which forms the inlet die, on the imposed pressure for a given fiber speed. Clearly, the pressure flattens and moves the meniscus upward, imparting greater stability to it and reducing the chances of a breakdown [25].

The flow and heat transfer in the coating applicator and die have also been investigated numerically. The shape of the meniscus was prescribed on the basis of experimental data and axisymmetric transport was assumed. The typical height of the meniscus was found to vary from around 10 μm to 100 μm. Typical

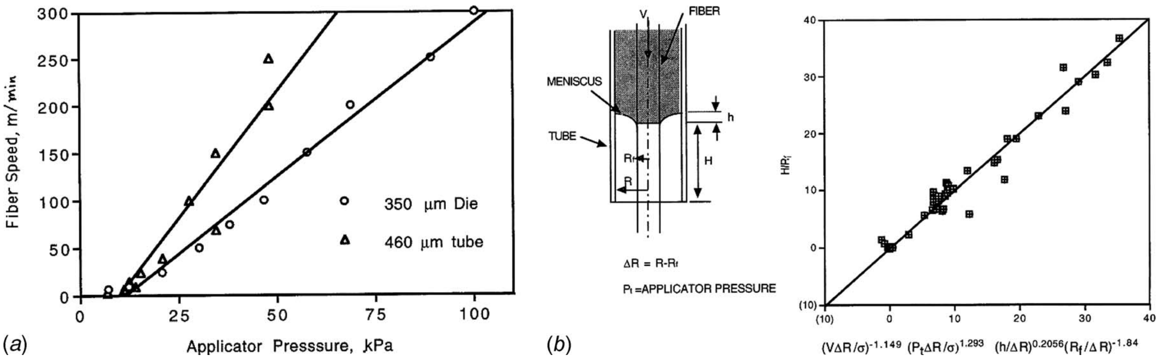

Fig. 15 (*a*) Dependence of fiber speed, for breakdown for a fiber entering a microchannel inlet, on the imposed pressure; (*b*) location of the meniscus in the microchannel as function of the pressure

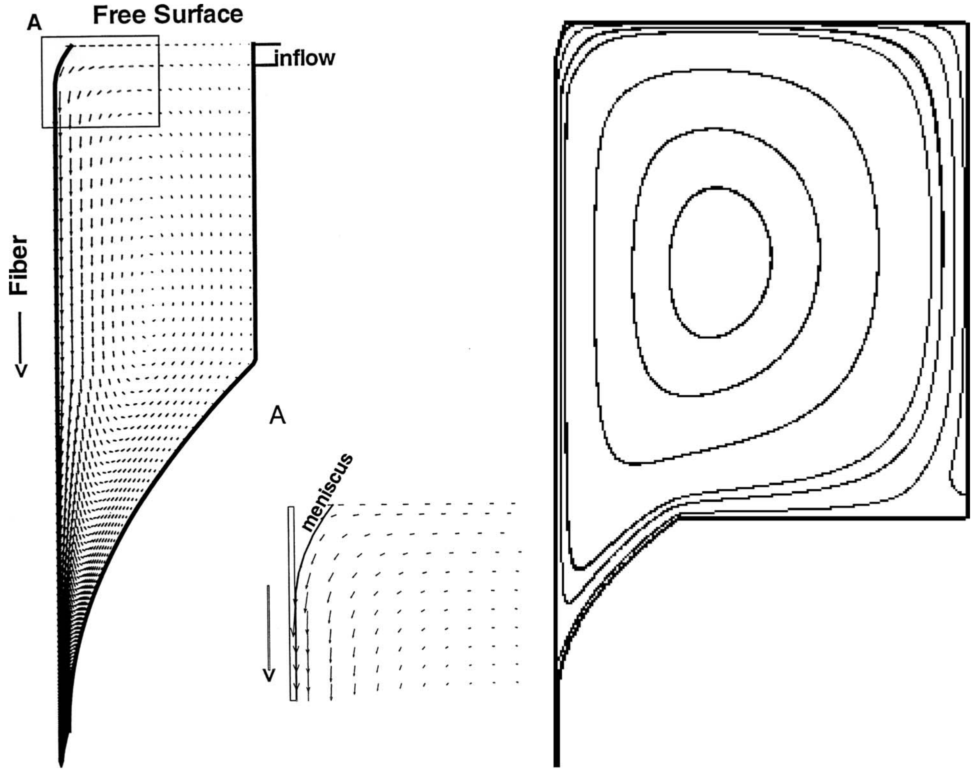

(*a*) (*b*)

Fig. 16 Calculated flow field in the applicator and exit microchannel, with a prescribed meniscus of height around 100 μm obtained experimentally

numerical results are shown here from Yoo and Jaluria [26] and Ravinutala et al. [27]. Figure 16 shows the computed velocity field in the applicator, with a prescribed upper meniscus. Thus, experimental inputs on the microscale phenomena underlying the meniscus are used to allow simulation of the macroscale flows. Even though the flow near the meniscus changed substantially with a change in the meniscus, the flow far away remained largely unaffected. A nanosecond double pulse laser source was used to map and probe the flow field in the applicator, particularly in the vicinity of the moving 125 μm fiber, using particle image velocimetry. Figure 17 shows a typical comparison between the two in terms of the velocity profiles. Several other such measurements and computations were carried out. The agreement between the two provided strong support to the modeling effort.

As mentioned earlier, the exit die consists of a microchannel of varying cross section. In most cases, it is a converging channel to the desired final diameter of the coating, though different geometries are used for stability and better control over coating characteristics. Figure 18 shows typical results obtained in terms of the pressure distribution in the applicator and the exit die for isothermal conditions. It is seen that a maximum arises somewhere near the midsection of the die. This pressure was found to be quite large due to the small diameter of the microchannel and to be much larger than the typical pressure imposed at the fluid inlet to the applicator. Thus, the exit conditions are largely dominated by the die shape and fiber speed, rather than the pressure in the applicator chamber. A properly designed die can help in controlling the thickness and quality of the coating. Thermal effects can also have a strong effect on the flow due to the dependence of fluid properties on temperature. The corresponding pressure distribution when thermal effects due to heat transfer from the fiber, viscous dissipation, and heat loss to the surroundings are included is shown in Fig. 18(*b*). The pressures were found to decrease as the temperatures increase due to the reduction in fluid viscosity. The flow was also found to be more stable, leading to greater uniformity of the coating, as the temperatures were increased. Thus, the thermal conditions at the boundaries can be used to affect the coating characteristics.

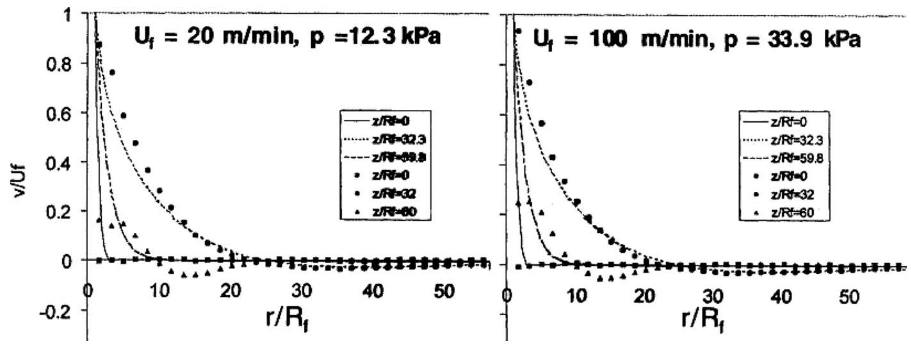

Fig. 17 Calculated and measured velocity distributions near the moving optical fiber

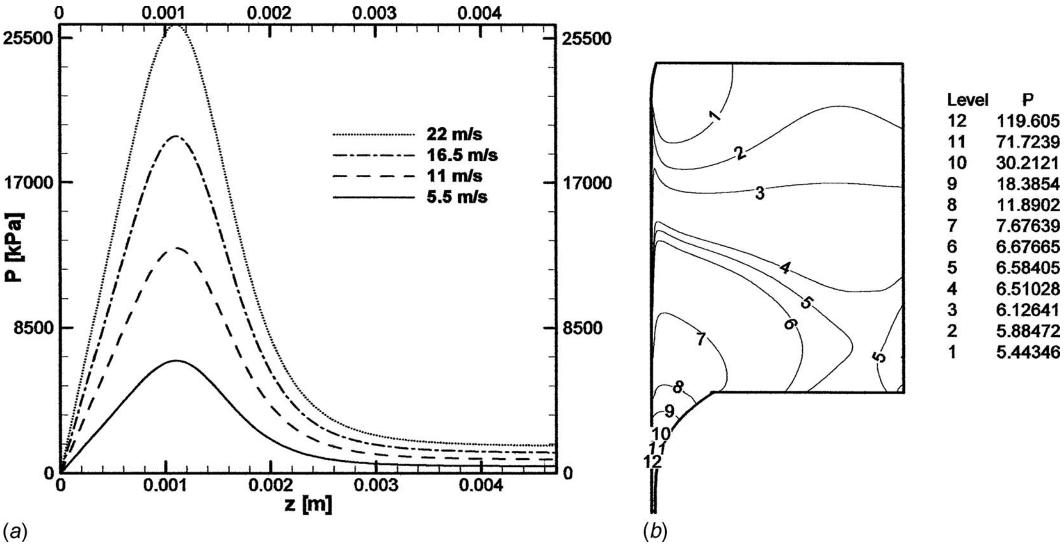

Fig. 18 Pressure distribution in the chamber and the exit die, which consists of a converging microchannel, for polymer coating of a moving fiber (*a*) under isothermal conditions and (*b*) when thermal effects are included for a fiber speed of 11 m/s

2.4 Chemical Vapor Deposition. Chemical vapor deposition involves the deposition of thin films from a gas phase on to a solid substrate by means of a chemical reaction that takes place during the deposition process. The activation energy needed for the chemical reactions is provided by an external heat source; see Fig. 19(*a*). The products of the reactions form a solid crystalline or an amorphous layer on the substrate. After material deposition on the surface, the byproducts of the reactions are removed by carrier gases, as reviewed by Mahajan [28]. Film thicknesses range from a few nanometers to tens of microns. The quality of the film deposited is characterized in terms of its purity, composition, thickness, adhesion, surface morphology, and crystalline structure. The level of quality needed depends on the intended application, with electronic and optical materials imposing the most stringent demands. This technique has become quite important in materials processing and is used in a wide range of applications, such as those in the fabrication of microelectronic circuits, optical and magnetic devices, high performance cutting and grinding tools, and solar cells. Much of the initial effort on this problem was directed at silicon deposition because of its importance in the semiconductor industry. However, recent efforts have been directed at the deposition of materials such as titanium nitride, silicon carbide, diamond, and metals such as titanium, tungsten, aluminum, and copper.

Many different types of CVD reactors have been developed and applied for different applications. The quality, uniformity, and rate of deposition are dependent on the heat and mass transfer, and on the chemical reactions that are themselves strongly influenced by temperature and concentration levels. The flow, heat transfer, and chemical reactions in CVD reactors have been investigated by several researchers [29–31]. Some typical results obtained for silicon deposition are shown in Fig. 19(*b*), indicating a comparison between numerical and experimental results from Ref. [29]. A fairly good agreement is observed, given the uncertainty with material property data and with the chemical kinetics. The two results from Ref. [32] are labeled as present and refer to two different values of the diffusion coefficient; the one labeled as the reference case employs the same values as those in Ref. [30].

2.5 Summary. Several important and interesting aspects, as well as challenges, have been brought out in the preceding discussion. Because of the need to determine temperature and flow dif-

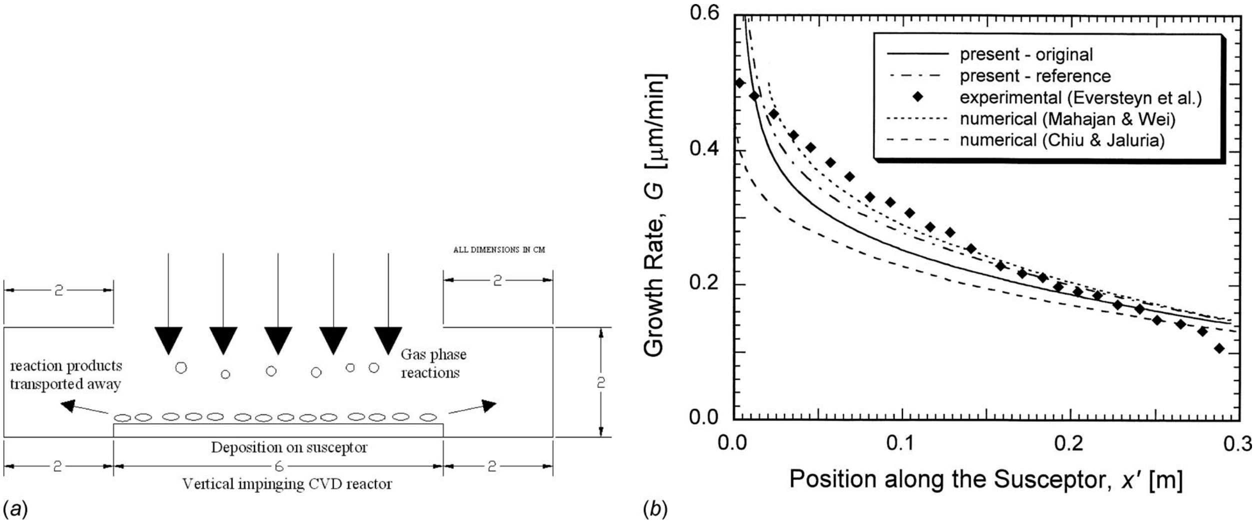

Fig. 19 (*a*) A sketch of an impingement type CVD reactor; (*b*) comparison between numerical predictions and experiments for chemical vapor deposition of silicon in a horizontal reactor

ferentials over very short distances, it is often not possible to treat the microscale region as uniform or lumped, making it necessary to place a substantial number of grid points over microscale dimension for an accurate and realistic numerical simulation. Viscous dissipation effects are large locally due to the small length scales. Similarly, large pressure differences arise in flows through microchannels. Large changes in length scale are often encountered in materials processing, going from several centimeters to micrometers in a short physical distance, as seen in optical fiber drawing. The traditional analysis, with no-slip conditions, is valid in many cases, particularly with liquids over lengths scales ranging down to a few microns. The experiments are usually much more involved than in commercial scales due to the device size and positioning of the probe. Validation of the models similarly becomes complicated because of the complexity of the experiments and because many experimental data are available at the macroscale or system level. A coupling between the different scales, therefore, becomes critical.

3 Underlying Processes That Occur at Micro/Nanoscale

3.1 Nano-, Micro-, and Macroscale Coupling. The characteristics and quality of the material being processed are generally determined by the transport processes that occur at the micro- or nanometer scale in the material, for instance, at the solid-liquid interface in casting or crystal growing, over molecules involved in a chemical reaction in chemical vapor deposition and reactive extrusion, or at sites where defects are formed in an optical fiber. However, engineering aspects are generally concerned with the commercial or macroscale, involving practical dimensions, systems, and appropriate boundaries. Therefore, it is crucial to link the two approaches so that the appropriate boundary conditions for a desired micro- or nanostructure can be imposed in a physically realistic system. A considerable interest exists today in this aspect of materials processing. For instance, interest lies in understanding microscopic phenomena associated with solidification, and intense research work has been directed at this problem. The solidification front can be divided into various morphological forms such as planar, cellular, and dendritic. Various models have been proposed and experiments carried out to characterize such structures and growth [33]. This includes, for instance, equiaxed and columnar dendritic crystals. Averaging volumes and dendrite envelopes that may be used for modeling of the microscopic phenomena are developed.

The properties of the material undergoing thermal processing must be known and appropriately modeled to accurately predict the resulting flow and transport, as well as the characteristics of the final product. However, there is an acute lack of data and the accuracy of the numerical simulation is often constrained due to the unavailability of material properties. Numerical modeling yields the prediction of the thermal history of the material as it undergoes a given thermal process. Similarly, the pressure, stress, mass transfer, and chemical reactions can be determined. The next step is to determine the changes in the structure or composition of the material as it goes through the system. But this requires detailed information on material behavior and how structural or chemical changes occur in the material as a consequence of the temperature, pressure, and other conditions to which it is subjected. A few examples that involve these considerations are outlined here.

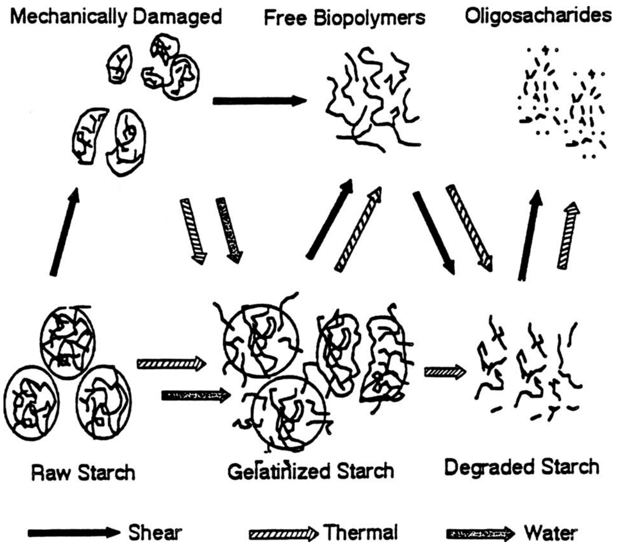

Fig. 20 A schematic indicating the mechanisms underlying starch conversion

3.2 Chemical Conversion in Biopolymers. In reactive thermal processing, such as food and reactive polymer extrusion, the microscopic changes in the material are linked with the operating conditions that are imposed on the system. A simple approach to model the chemical conversion process in reactive materials, such as food, is based on the governing equation for chemical conversion, given as [34]

$$\frac{d}{dt}[(1-X)] = -K(1-X)^m \tag{10}$$

where X is the degree of conversion, defined as

$$X = \frac{M_i - M_t}{M_i - M_f} \tag{11}$$

Here M_i is the initial amount of unconverted material, taken as starch here, M_f is the final amount of unconverted starch, and M_t is the amount of unconverted starch at time t. The order of the reaction is m and K is the reaction rate, these generally being determined experimentally using a digital scanning calorimeter. The order of the reaction m in Eq. (10) has been shown to be zero for starches and the rate of the reaction K given as a combination of thermal (T) and shear (S) driven conversion as

$$K = K_T + K_S \tag{12}$$

$$\text{where} \quad K_T = K_{To}\exp(-E_T/RT), \quad K_S = K_{So}\exp(-E_S/\tau\eta) \tag{13}$$

Here, τ is the shear stress, and η is a constant, which is obtained experimentally for the material, along with other constants in the equation. Figure 20 shows these mechanisms qualitatively in the form of a schematic. A simple approximation may be applied to model the degree of conversion defined in Eq. (11), as given by [35]

$$w\frac{dX}{dz} = K \tag{14}$$

Here, w is the velocity in the down-channel direction z in an extruder. Thus, numerical results on conversion in the channel are obtained by integrating this equation.

Using the microscale conversion mechanisms given above, the flow, heat transfer, and conversion in a screw extruder can be obtained. The viscosity is a function of the conversion and this complicates the physical process, as well as the simulation. Figure 21 shows some typical results obtained from such a simulation [36]. Figure 21(a) shows the temperature field and the conversion in a tapered single-screw extruder. As expected, conversion increases as the flow goes from the inlet to the outlet at the die. Figure 21(b) shows the feasible domain for a twin-screw extruder with Amioca, or pure starch, as the extruded material. The feasibility of the process is determined largely by the flow and the pressure and temperature rise in the extruder. An upper limit is

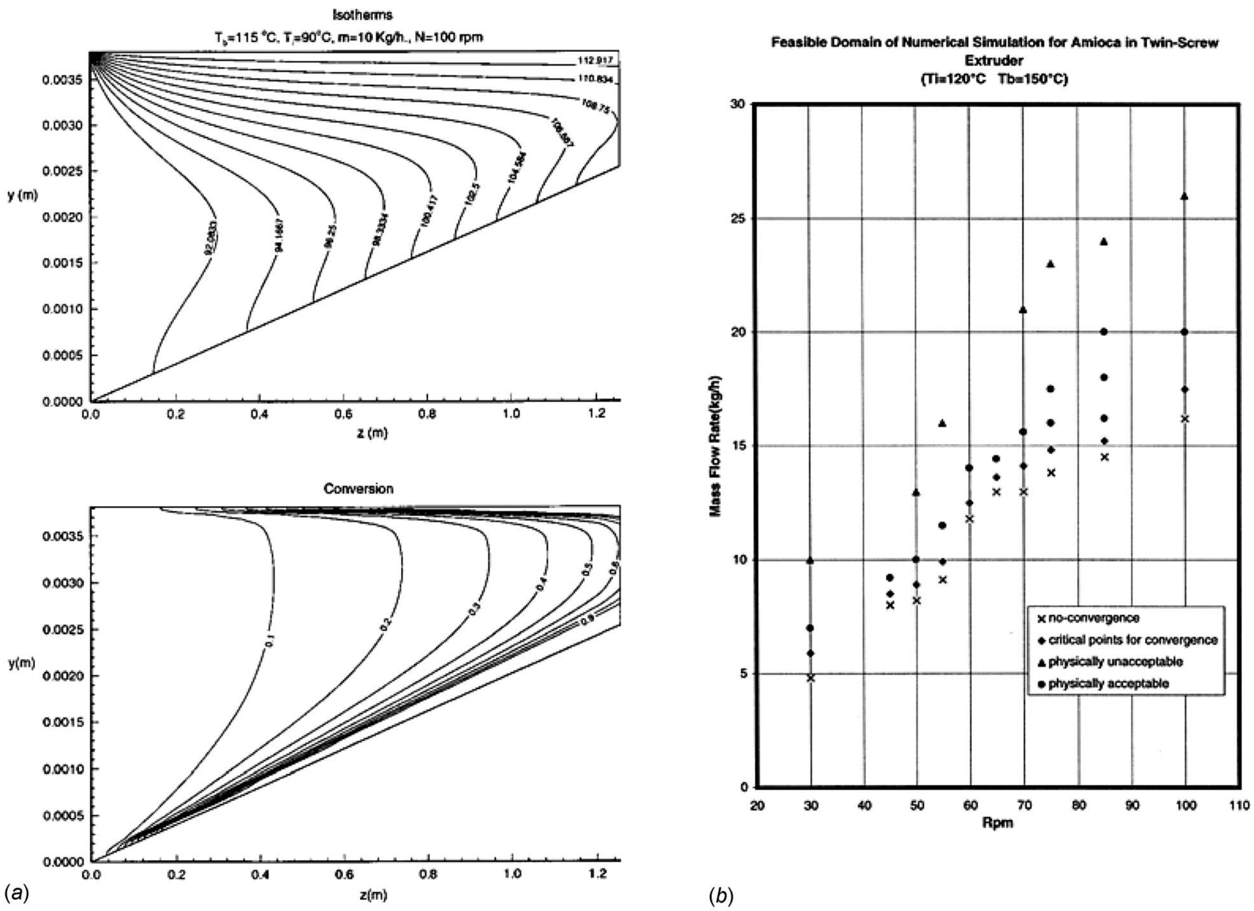

Fig. 21 (*a*) **Conversion of starch in a tapered screw extruder channel;** (*b*) **feasible domain for twin-screw extrusion of starch**

obtained for the mass flow rate, beyond which it is necessary to impose a favorable pressure gradient to push the material down the channel. Therefore, a negative pressure gradient along the axial direction will occur in the channel and that is not physically acceptable for an extruder. A lower limit on mass flow rate is also obtained because of recirculation of the flow, which makes the process unstable and leads to high pressures and material degradation. Thus, a fairly narrow range of mass flow rates yields a feasible extrusion process.

3.3 Thermally Induced Defects.

Another area in which the changes at the molecular level are considered is that of generation of thermally induced defects in optical fiber drawing. The differential equation for the time dependence of the E' defect concentration was formulated by Hanafusa et al. [37] based on the theory of the thermodynamics of lattice vacancies in crystals. The E' defect is a point defect, which is generated at high temperature during the drawing process and which causes transmission loss and mechanical strength degradation in the fiber. It was assumed that the E' defects are generated through breaking of the Si–O band, and, at the same time, part of the defects recombine to form Si–O again. The net concentration of the E' defects is the difference between the generation and the recombination. The equation for E' defect concentration is given as [37]

$$v\frac{dn_d}{dz} = n_p(0)v\,\exp\left(-\frac{E_p}{KT}\right) - n_d v\left[\exp\left(-\frac{E_p}{KT}\right) + \exp\left(-\frac{E_d}{KT}\right)\right] \tag{15}$$

where n_d and E_d represent the concentration and activation energy of the E' defect, and n_p and E_p represent those of the precursors. The initial values and constants are defined as [37] $n_d(0)=0$, $n_p(0)=7\times10^{22}\ \mathrm{g}^{-1}$, $E_p=6.4087\times10^{-19}$ J, $E_d=0.3204\times10^{-19}$ J, $v=8\times10^{-3}\ \mathrm{s}^{-1}$, and $K=1.380658\times10^{-23}$ J/K.

Figure 22(*a*) shows the dependence of the average concentration of E' defects on the drawing temperature, indicating an increase with temperature as expected from the higher breakage of the Si–O bond. Figure 22(*b*) shows the final concentration of the defects as obtained from the luminescence of the fibers. If the fiber is rapidly cooled slowly after the draw furnace, the defects are reduced due to the annealing of the fiber resulting in recombination of the broken bonds. If they are cooled very fast by forced convection, the defects are frozen and yield a higher concentration. Again, these effects arise due to the microscopic mechanisms operating at the level of the defects. Figure 23 shows the neck-down profile and the defects for a doped fiber. As expected, the concentration of E' defects is found to be larger in the double-layer preform due to higher temperatures, as seen earlier. It is indicated that the fiber quality is degraded with an increase in refractive index difference between the core and the cladding in terms of E' defects.

3.4 CVD Thin Film Deposition.

Similarly, chemical kinetics plays a critical role in the deposition of material from the gas phase in chemical vapor deposition systems [28]. The concentrations of the chemical species in the reactor affect the chemical kinetics, which in turn affect the deposition. In many cases, the process is chemical kinetics limited, implying that the transport processes are quite vigorous and the deposition is restricted largely by the kinetics. The chemical kinetics for several materials is available in literature. For instance, the chemical kinetics for the

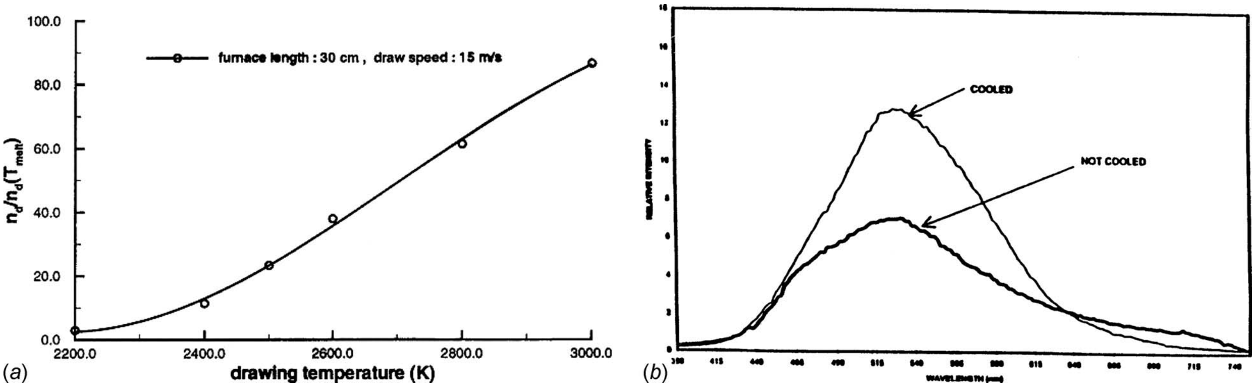

Fig. 22 (***a***) **Dependence of average concentration of *E′* defects on furnace wall temperature; (*b*) luminescence versus wavelength of fibers drawn at 2050°C and 80 m/min, indicating concentration of *E′* defects**

deposition of silicon from silane (SiH_4) with hydrogen as the carrier gas in a CVD reactor is given by the expression [29]

$$K = \frac{K_0 p_{SiH_4}}{1 + K_1 p_{H_2} + K_2 p_{SiH_4}} \tag{16}$$

where the surface reaction rate K is in mole of Si/m^2 s, $K_0 = A \exp(-E/RT)$, E being the activation energy, and A, K_1, and K_2 are constants that are obtained experimentally. The ps are the partial pressures of the two species in the reactor.

Figure 24 shows the deposition characteristics for silicon at various susceptor temperatures and inlet velocities. At high temperatures, the surface reactions are fast and all the reactants reaching the surface get consumed by the surface reactions. The diffusion or transport of the reactant species to the substrate then becomes the limiting step. At low flow velocities, the gas stream has sufficient residence time to equilibrate with the substrate surface. The deposition rate then increases with flow rate. At high flow velocities, the surface concentrations cannot quickly adapt to the flow of products in the deposition zone and diffusion becomes the controlling factor. At sufficiently high flow velocities, the decomposition becomes kinetically controlled and is independent of the total flow rate. The variation of deposition uniformity with the susceptor temperature for various inlet velocities is also shown. The lower the value of the logarithm of the uniformity parameter U_p, the better the uniformity of the film thickness. Thus, the process can be optimized to obtain high uniformity and high deposition rates.

3.5 Summary. It is seen that transport processes occurring at micro- or nanometer scale determine the resulting characteristics of the material undergoing thermal processing. However, the operating conditions are generally imposed at macroscale, or at the system level. Therefore, it is important to study the processes at the microscale level and link these with the conditions at the macroscale. From the few examples discussed, it is seen that experimental results at microscale, or smaller dimensions, can often be employed, along with numerical modeling at larger scales. Analysis can also be used at the molecular level, as done for thermally induced defects, to obtain the inputs for the overall model.

4 Conclusions and Future Research Needs

This paper presents a review on microscale transport involved with thermal processing of materials. It focuses on two major aspects. The first concerns devices and applications that occur in the microscale range. The second deals with underlying microscale mechanisms that affect the characteristics of the material undergoing processing. Important challenges that arise when dealing with microscale devices are discussed. These include modeling and numerical simulation, which are similar to those at macroscale if the dimensions are typically much larger than the mean free path of the energy carriers in the fluid, the extensive care needed to obtain accurate experimental results at these small scales, the special instrumentation frequently needed to study basic processes, and validation of the models since imposed boundary conditions are largely at macroscale. Important considerations

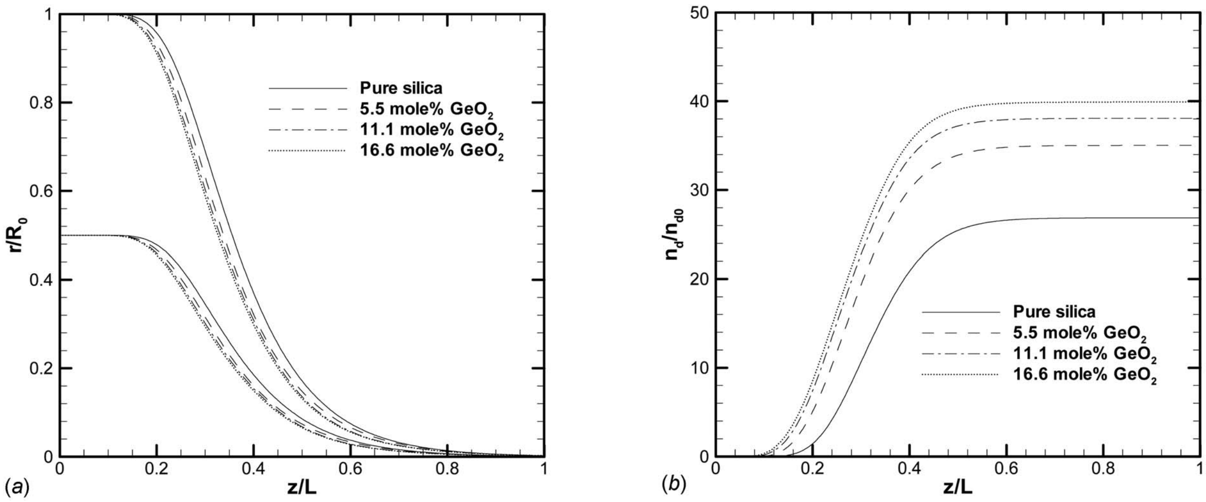

Fig. 23 (***a***) **Neck-down profiles for various GeO_2 concentrations; (*b*) concentration of *E′* defects along the centerline for various GeO_2 concentrations**

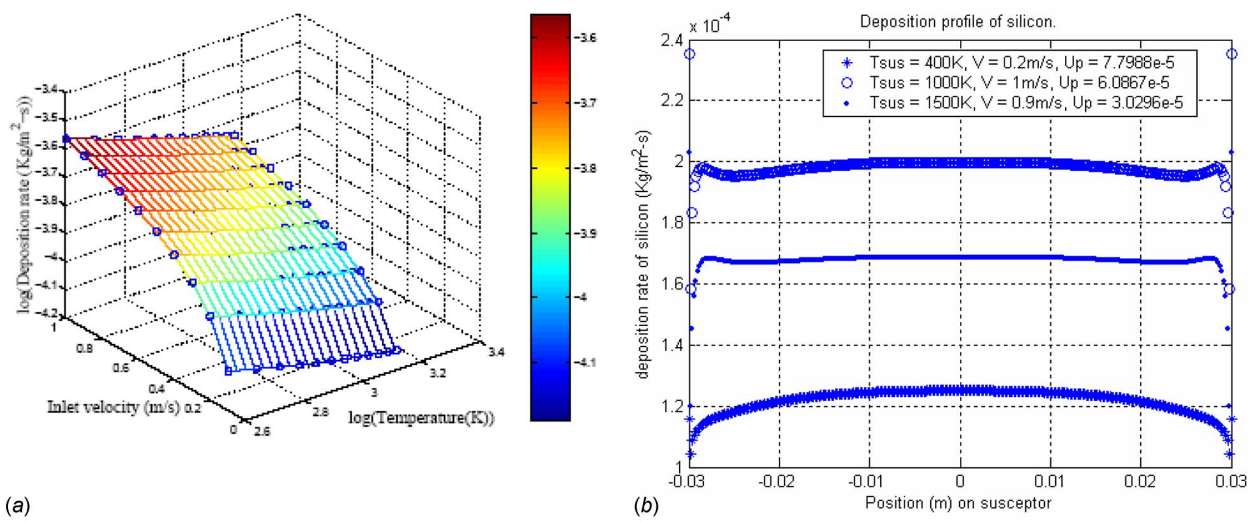

Fig. 24 (*a*) **Response surface on deposition rate for an impingement CVD reactor for depositing silicon;** (*b*) **variation of deposition rate with location for different inlet velocities and susceptor temperatures**

that are of particular significance at these dimensions, such as surface tension effects, high viscous dissipation, and high pressures needed for flow in microchannels, are discussed, in terms of several examples of thermal materials processing. Since processes at micro- and nanoscale strongly affect product quality, the review next discusses experiments often needed to characterize material changes, thermally induced defects generated, local stresses, and other imperfections. The effects on material and product characteristics are outlined, along with the link between micro- or nanoscale processes and operating conditions imposed at macroscale. Again, several examples from processes such as optical fiber drawing, thin film deposition, and reactive extrusion are taken to present the basic approach and typical results. The further work needed on process simulation, feasibility, control, design and optimization, material characterization, and experimentation for validation and insight at microscale is briefly discussed in terms of the thermal processing of advanced materials and devices.

Acknowledgment

The author acknowledges the support of the National Science Foundation, through several grants, of the Fiber Optic Materials Research Program at Rutgers University, and of Corning, Inc., for donated equipment. The author also acknowledges the interactions with Professor C. Polymeropoulos, Professor George Sigel, Professor M.V. Karwe, and Professor H.C. Gea, and the work done by several students, as referenced here, that made it possible to carry out this work and thus present this review.

Nomenclature

a = absorption coefficient
C = collapse ratio in hollow fiber drawing
c_p = specific heat at constant pressure
H = height
J = radiosity
K = thermal conductivity
L = preform length
n = refractive index, power-law index
p = pressure
q = heat flux
r = radial coordinate distance
R = radius
S_r = radiation source term
t = time
T = temperature
u = radial velocity
v = axial velocity
z = axial coordinate distance

Greek Symbols

ε = emissivity
λ = wavelength
μ = dynamic viscosity
υ = kinematic viscosity
Φ = viscous dissipation term
ρ = density, reflectivity
τ = shear stress, transmissivity
$\dot{\gamma}$ = shear rate
σ = Stefan–Boltzmann constant
ζ = surface tension

Subscripts

f = fiber
F = furnace
0 = preform inlet
C = centerline

Superscripts

(1) = core, inner surface
(2) = cladding, outer surface
(3) = gas

References

[1] Jaluria, Y., 2003, "Thermal Processing of Materials: From Basic Research to Engineering," ASME J. Heat Transfer, **125**, pp. 957–979.
[2] Jaluria, Y., 2006, "Numerical Modeling of Manufacturing Processes," *Handbook of Numerical Heat Transfer*, W. J. Minkowycz, E. M. Sparrow, and J. Murthy, eds., Wiley, New York, pp. 729–784.
[3] Szekely, J., 1979, *Fluid Flow Phenomena in Metals Processing*, Academic, New York.
[4] Viskanta, R., 1988, "Heat Transfer During Melting and Solidification of Metals," ASME J. Heat Transfer, **110**, pp. 1205–1219.
[5] Li, T., ed., 1985, *Optical Fiber Communications*, Vol. 1, Academic, New York.
[6] Poulikakos, D., ed., 1996, "Transport Phenomena in Materials Processing," Adv. Heat Transfer, **28**, pp. 1–425.
[7] Paek, U. C., 1999, "Free Drawing and Polymer Coating of Silica Glass Optical Fibers," ASME J. Heat Transfer, **121**, pp. 774–788.
[8] Fitt, A. D., Furusawa, K., Monro, T. M., and Please, C. P., 2001, "Modeling the Fabrication of Hollow Fibers: Capillary Drawing," J. Lightwave Technol., **19**, pp. 1924–1931.
[9] van Eijkelenborg, M. A., Argyros, A., Barton, G., Bassett, I. M., Fellew, M., Henry, G., Issa, N. A., Large, M. C. J., Manos, S., Padden, W., Poladian, L., and Zagari, J., 2003, "Recent Progress in Microstructured Polymer Optical Fibre Fabrication and Characterisation," Opt. Fiber Technol., **9**, pp. 199–209.

[10] Paek, U. C., and Runk, R. B., 1978, “Physical Behavior of the Neck-Down Region During Furnace Drawing of Silica Fibers,” J. Appl. Phys., **49**, pp. 4417–4422.

[11] Myers, M. R., 1989, “A Model for Unsteady Analysis of Preform Drawing,” AIChE J., **35**, pp. 592–602.

[12] Lee, S. H.-K., and Jaluria, Y., 1997, “Simulation of the Transport Process in the Neck-Down Region of a Furnace Drawn Optical Fiber,” Int. J. Heat Mass Transfer, **40**(4), pp. 843–856.

[13] Choudhury, R. S., and Jaluria, Y., 1998, “Thermal Transport Due to Material and Gas Flow in a Furnace for Drawing an Optical Fiber,” J. Mater. Res., **13**(2), pp. 494–503.

[14] Choudhury, R. S., Jaluria, Y., and Lee, S. H.-K., 1999, ““A Computational Method for Generating the Free-Surface Neck-Down Profile for Glass Flow in Optical Fiber Drawing,” Numer. Heat Transfer, Part A, **35**, pp. 1–24.

[15] Yin, Z., and Jaluria, Y., 1998, “Thermal Transport and Flow in High-Speed Optical Fiber Drawing,” ASME J. Heat Transfer, **120**, pp. 916–930.

[16] Wei, Z., Lee, K., Tchikanda, S. W., Zhou, Z., and Hong, S., 2004, “Free Surface Flow in High Speed Fiber Drawing With Large-Diameter Glass Preforms,” ASME J. Heat Transfer, **126**, pp. 713–722.

[17] Cheng, X., and Jaluria, Y., 2004, “Feasibility of High Speed Furnace Drawing of Optical Fibers,” ASME J. Heat Transfer, **126**, pp. 852–857.

[18] Paek, U. C., 1986, “High-Speed High-Strength Fiber Drawing,” J. Lightwave Technol., **4**(8), pp. 1048–1060.

[19] Chen, C., and Jaluria, Y., 2007, “Numerical Simulation of Transport in Optical Fiber Drawing With Core-Cladding Structure,” ASME J. Heat Transfer, **129**, pp. 559–567.

[20] Izawa, T., and Sudo, S., 1987, *Optical Fibers: Materials and Fabrication*, KTK Scientific, Tokyo.

[21] Chen, C., 2007, “Transport Processes in Drawing of Optical Fibers With Core-Cladding Structure,” Ph.D. thesis, Rutgers University, New Brunswick, NJ.

[22] Chakravarthy, S. S., and Chiu, W. K. S., 2005, “Collapse Prediction During Hollow Optical Fiber Fabrication,” 2005 ASME Summer Heat Transfer Conference, San Francisco, CA.

[23] Yang, Y., and Jaluria, Y., 2008, “Transport Processes Governing the Drawing of a Hollow Optical Fiber,” ASME Summer Heat Transfer Conference, Jacksonville, FL.

[24] Quere, D., 1999, “Fluid Coating on a Fiber,” Annu. Rev. Fluid Mech., **31**, pp. 347–384.

[25] Ravinulata, S., and Polymeropoulos, C. E., 2002, “Entrance Meniscus in a Pressurized Optical Fiber Coating Applicator,” Exp. Therm. Fluid Sci., **26**, pp. 573–580.

[26] Yoo, S. Y., and Jaluria, Y., 2007, “Fluid Flow and Heat Transfer in an Optical Fiber Coating Process,” Int. J. Heat Mass Transfer, **50**, pp. 1176–1185.

[27] Ravinutala, S., Polymeropoulos, C. E., Jaluria, Y., Elliott, G., and Finberg, G., 2001, “Experimental and Calculated Velocity Distributions Within a Pressurized Optical Fiber Coating Applicator,” *Proceedings of the 50th International Wire Cable Symposium*, Orlando, FL.

[28] Mahajan, R. L., 1996, “Transport Phenomena in Chemical Vapor-Deposition Systems,” Adv. Heat Transfer, **28**, pp. 339–425.

[29] Eversteyn, F. C., Severin, P. J. W., Brekel, C. H. J., and Peek, H. L., 1970, “A Stagnant Layer Model for the Epitaxial Growth of Silicon From Silane in a Horizontal Reactor,” J. Electrochem. Soc., **117**, pp. 925–931.

[30] Mahajan, R. L., and Wei, C., 1991, “Buoyancy, Soret, Dufour and Variable Property Effects in Silicon Epitaxy,” ASME J. Heat Transfer, **113**, pp. 688–695.

[31] Chiu, W. K. S., and Jaluria, Y., 2000, “Continuous Chemical Vapor Deposition Processing With a Moving Finite Thickness Susceptor,” J. Mater. Res., **15**, pp. 317–328.

[32] Yoo, H., and Jaluria, Y., 2002, “Thermal Aspects in the Continuous Chemical Vapor Deposition of Silicon,” ASME J. Heat Transfer, **124**, pp. 938–946.

[33] Beckermann, C., and Wang, C. Y., 1995, “Multiphase/-Scale Modeling of Alloy Solidification,” Annu. Rev. Heat Transfer, **6**, pp. 115–198.

[34] Wang, S. S., Chiang, C. C., Yeh, A. I., Zhao, B., and Kim, I. H., 1989, “Kinetics of Phase Transition of Waxy Corn Starch at Extrusion Temperatures and Moisture Contents,” J. Food. Sci., **54**, pp. 1298–1301.

[35] Chiruvella, R. V., Jaluria, Y., and Karwe, M. V., 1996, “Numerical Simulation of Extrusion Cooking of Starchy Materials,” J. Food. Eng., **30**, pp. 449–467.

[36] Zhu, W., and Jaluria, Y., 2001, “Residence Time and Conversion in the Extrusion of Chemically Reactive Materials,” Polym. Eng. Sci., **41**, pp. 1280–1291.

[37] Hanafusa, H., Hibino, Y., and Yamamoto, F., 1985, “Formation Mechanism of Drawing-Induced E’ Centers in Silica Optical Fibers,” J. Appl. Phys., **58**(3), pp. 1356–1361.